Quality-controlled meteorological datasets from SIGMA automatic weather stations in northwest Greenland, 2012–2020

Motoshi Nishimura[1*], Teruo Aoki[1], Masashi Niwano[2], Sumito Matoba[3], Tomonori Tanikawa[2], Tetsuhide Yamasaki[4], Satoru Yamaguchi[5], Koji Fujita[6]

[1]National Institute of Polar Research, Tokyo, Japan

[2]Meteorological Research Institute, Japan Meteorological Agency, Ibaraki, Japan

[3]Institute of Low Temperature Science, Hokkaido University, Hokkaido, Japan

[4]Avangnaq Arctic Project, Osaka, Japan

[5]Snow and Ice Research Center, National Research Institute for Earth Science and Disaster Resilience, Niigata, Japan

[6]Graduate School of Environmental Studies, Nagoya University, Nagoya, Japan

Correspondence to: Motoshi Nishimura (nishimura.motoshi@nipr.ac.jp)

Abstract. In situ meteorological data are essential to better understand ongoing environmental changes in the Arctic. Here, we present a dataset of quality-controlled meteorological observations by two automatic weather stations in northwest Greenland from July 2012 to the end of August 2020. The stations were installed in the accumulation area on the Greenland Ice Sheet (SIGMA-A site, 1490 m a.s.l.) and near the equilibrium line of the Qaanaaq Ice Cap (SIGMA-B site, 944 m a.s.l.). We describe the two-step sequence of quality-control procedures that we used to create increasingly reliable datasets by masking erroneous data records. Those data sets are archived in the Arctic Data archive System (ADS) (SIGMA-A; http://doi.org/10.17592/001.2022041303, SIGMA-B; http://doi.org/10.17592/001.2022041306). We analyzed the resulting 2012–2020 time series of air temperature, surface height, surface albedo, and histograms of longwave radiation (a proxy of cloud formation frequency). We found that surface height increased and albedo remained steady at the SIGMA-A site, whereas high air temperatures and clear-sky conditions prevailed while surface height was significantly lowering and albedo decreased in the summers of 2015, 2019, and 2020 at the SIGMA-B site. Therefore, it appears that these weather conditions led to apparent surface height decrease at the SIGMA-B site but not at the SIGMA-A site. We anticipate that this quality-control method and these datasets will aid in climate studies of northwest Greenland as well as contribute to the advancement of broader polar climate studies.

1. Introduction

Automatic weather observation in Greenland started with GC-Net (Greenland Climate Network; Steffen and Box, 2001), which was established as a network of automatic weather stations (AWS) in Greenland after 1990. This observation network intended to provide long-term observations of climatological and glaciological factors over Greenland. This was followed by the PROMICE (van As et al., 2011; Fausto et al., 2021) led by the Geological Survey of Denmark and Greenland (GEUS) and the K-transect network (van de Wal et al., 2005), led by Utrecht University in the Netherlands, has been deployed. PROMICE is currently operating the largest observation network in Greenland by contracting the maintenance of GC-Net equipment, and K-transect has deployed equipment mainly in the western part of the country and continues to monitor the area closely. Both networks have provided important long-term meteorological data.

To contribute to these efforts and to fill a spatial gap, we established two AWS systems in northwest Greenland (Fig. 1), where rapid environmental changes have occurred in recent years (Aoki et al., 2014). Recent studies of this region have documented a drastic mass loss since the mid-2000s (Mouginot et al., 2019), an expansion of the ablation area (Noël et al., 2019), and a hot spot of increasing rainfall (Niwano et al., 2021). The two sites were established in 2012 as a part of the Snow Impurity and Glacial Microbe effects on abrupt warming in the Arctic (SIGMA) Project, which aimed to clarify the dramatic enhancement of melting of the Greenland Ice Sheet induced by snow impurities (e.g., black carbon, mineral dust). The observational data acquired since that time have been used by glaciological (Yamaguchi et al., 2014; Tsutaki et al., 2017; Matoba et al., 2018; Kurosaki et al., 2020), meteorological (Aoki et al., 2014; Tanikawa et al., 2014; Niwano et al., 2015; Hirose et al., 2021), and biological studies (Onuma et al., 2018; Takeuchi et al., 2018). These data are also valuable because they support the output of numerical models (e.g., Niwano et al., 2018; Fujita et al., 2021) and form the basis for robust analytical results.

The datasets from AWS generally contain erroneous data records that are attributed to natural factors (e.g., riming, ice accretion, snow accumulation on sensors) or "Zero Offset" (Behrens, 2021) for radiation sensors. Various procedures exist for improving the accuracy of such datasets (e.g., Fiebrich et al., 2010; Fausto et al., 2021). In particular, careful Quality Control (QC) procedures, which is a process to improve the quality of data by removing outliers, are required for downward radiation sensors, which are sensitive to solar zenith angle, icing, riming, and snowfall (van den Broeke et al., 2004a, b; Moradi, 2009). Other QC procedures deal with error sources through range, step, and internal consistency tests (Estévez et al., 2011). The specifics of QC methods, for example, the threshold value for detecting erroneous data records, should be adjusted for each observation environment. In this paper, we describe the QC methods used for the in situ meteorological observation data from northwest Greenland, which include existing QC methods, new ones, and combinations of both.

After describing the AWS sites (Sect. 2) and their datasets (Sect. 3), this paper introduces the two

67 separate QC methods used sequentially to mask erroneous data records (Sect. 4). We then present
68 examples of time series of meteorological variables in northwest Greenland, infer their implications
69 for interannual variations in weather conditions, and describe the differences between the two sites
70 (Sect. 5).

2. AWS general description

72   The two AWSs are installed at the SIGMA-A site (78.052° N, 67.628° W; 1490 m a.s.l.), on the
73 northwest Greenland Ice Sheet, and the SIGMA-B site (77.518° N, 69.062° W; 944 m a.s.l.), on the
74 Qaanaaq Ice Cap, a peripheral ice cap on the Greenland coast (Fig. 1). They have been in operation
75 since July 2012 (Aoki et al., 2014). The observed parameters and those sensor specifications including
76 abbreviations are listed in Table 1, and the other key constants, variables, and their abbreviations used
77 in this study are also in Table 2.
78   The SIGMA-A site is 70 km inland from the coast on a ridge of the Greenland Ice Sheet extending
79 northwest from the Greenland Summit; it sits on a flat snow surface with no obstacles around the site
80 (see Fig. 2). This site is in an accumulation area for the ice sheet (Matoba et al., 2018) based on the
81 analysis of ice-core data (Yamaguchi et al., 2014; Matoba et al., 2017). The SIGMA-B site is 3 km
82 north of the village of Qaanaaq. This site is considered to be located at near the equilibrium line (910
83 m a.s.l.; Tsutaki et al., 2017) on the Qaanaaq Ice Cap, which ranges in elevation between 30 and 1110
84 m a.s.l. (Sugiyama et al., 2014). The surface condition at this site varies (see Fig. 2), and significant
85 surface height decreasing has occurred in warm years (e.g., Aoki et al., 2014). The site is on a
86 southwest-facing slope (azimuth 220°) with an angle of 4° according to 10 m DEM data (Porter et al.,
87 2018).
88
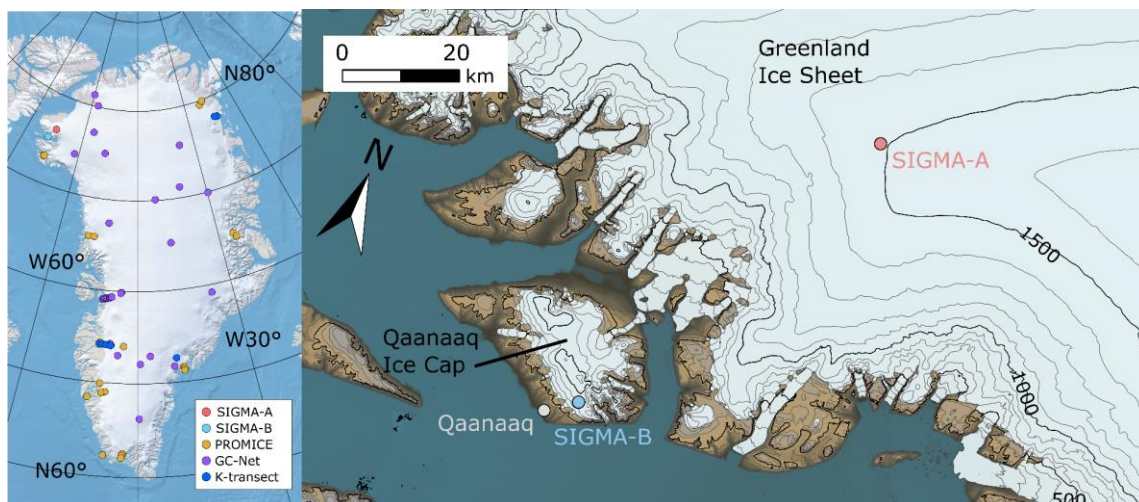
90 Figure 1. Location map of Greenland showing PROMICE, GC-Net, and K-transect AWS sites (left)

91 and a local map of northwest Greenland showing locations of AWS sites SIGMA-A and SIGMA-B.

92 Contour interval in the right panel is 100 m.

93
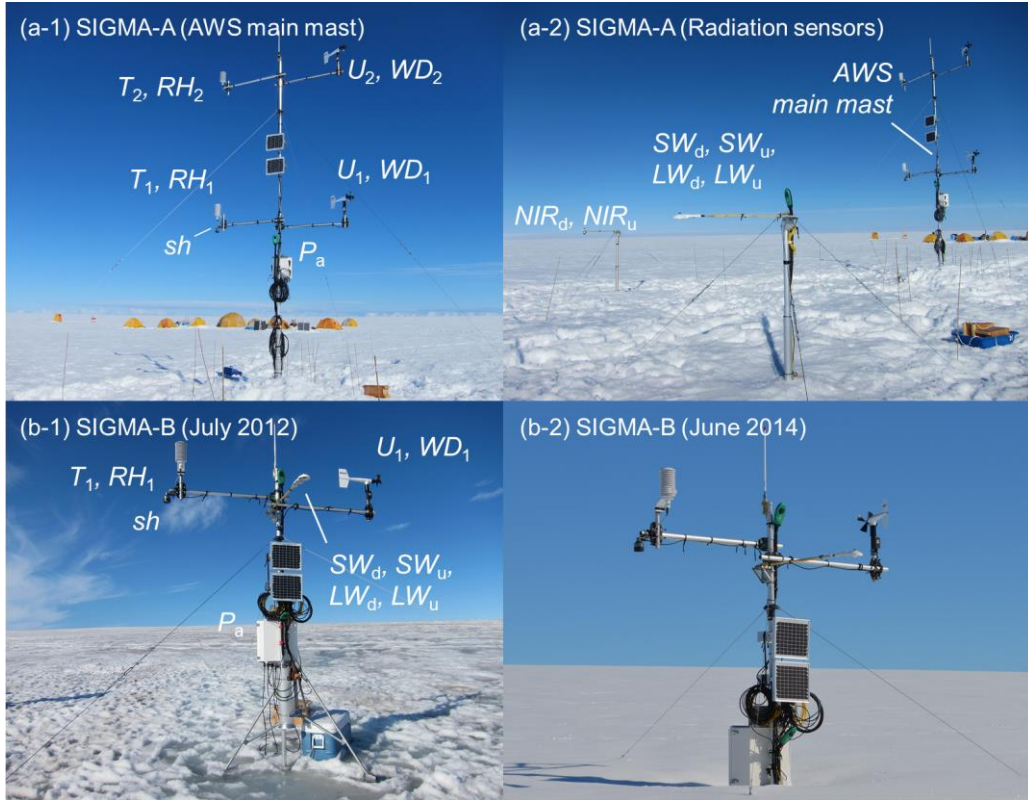
94

95 Figure 2. Setting and instrumentation at the SIGMA-A site (top) and the SIGMA-B site (bottom).

96 Surface conditions at SIGMA-B are shown in July 2012 and June 2014. Sensors are labeled with the

97 observation parameters they measure (see Table 1).

98

99 Table 1. Meteorological observation parameters and sensor specifications.

observation parameter	abbreviation	unit	sensor	observaion range	accuracy
wind speed	$U_n{}^a$	m s^{-1}	Young, 05103	0 to 100 [m s^{-1}]	± 0.3 m s^{-1} or 1%
wind direction	$WD_n{}^a$	degree	Young, 05103	360° mechanical, 355° electrical (5° open)	± 3°
air temperature	$T_n{}^a$	°C	Vaisala, HMP155^b	−80 to +60 [°C]	±0.17 °C
relative humidity^c	$RH_n{}^a$	%	Vaisala, HMP155^b	0 to 100%	±1% (0 to 90%) ±1.7% (90 to 100%)
atmospheric pressure	P_a	hPa	Vaisala, PTB210	500 to 1100 [hPa]	±0.30 hPa at 20 °C
downward and upward shortwave radiation	SW_d, SW_u	W m^{-2}	Kipp & Zonen, CNR4	0.3 to 2.8 [µm]	±5% (daily total)
downward and upward longwave radiation	LW_d, LW_u	W m^{-2}	Kipp & Zonen, CNR4	4.5 to 42 [µm]	±10% (daily total)
downward and upward near-infrared radiation	NIR_d, NIR_u	W m^{-2}	Kipp & Zonen, CMP6 with a RG715 cut-off filter	0.715 to 2.8 [µm]	±5% (daily total)
surface height	sh	cm	Campbell, SR50	0.5 to 10 [m]	1 cm or 0.4%
snow temperature	$st_n{}^a$	°C	Climatec, C-PTWP-10	−40 to +60 [°C]	±0.15°C
tilts of the main mast	$Tilt_X, Tilt_Y$	degree	TURCK, B2N85H-Q20L60-	−85° to +85°	±0.5°

a: "n" suffix is appended to distinguish the observation height or depth.
b: protected from direct solar irradiance by a naturally-aspirated 14-plate Gill radiation shield
c: Relative humidity is measured relative to water even in sub-freezing environments

100

101

102   Table 2. Key constants, variables, and their symbols used in this paper.

symbol	name	value	unit
constant			
f_{nir}	a fraction of near-infrared radiant flux in the shortwave radiant flux at the top of the atmosphere	0.5151	no dimension
I_0	solar constant	1361	$W\,m^{-2}$
n	cloud cover coefficient	0.5	no dimension
r_m	annual mean distance between the Sun and the Earth	1.496×10^8	km
$sh_{initial}$	initial height of the surface height sensor	300	cm
α_{sw_max}	maximum value of surface albedo	0.95	no dimension
α_{nir_max}	maximum value of surface near-infrared albedo	0.90	no dimension
κ	constant depending on cloud type	0.26	no dimension
ε	snow/ice surface emissivity	0.98	no dimension
σ	Stefan-Boltzmann constant	5.67×10^8	$W\,m^{-2}\,K^{-4}$
variable			
d	diffuse fraction in global radiation		no dimension
I_d	diffuse solar radiation		$W\,m^{-2}$
I_s	direct solar radiation		$W\,m^{-2}$
LW_d	downward longwave radiation		$W\,m^{-2}$
LW_{std}	standard atmospheric longwave radiation		$W\,m^{-2}$
LW_u	upward longwave radiation		$W\,m^{-2}$
NIR_d	downward near-infrared radiation		$W\,m^{-2}$
NIR_u	upward near-infrared radiation		$W\,m^{-2}$
P_a	atmospheric pressure		hPa
r	distance between the Sun and the Earth		m
$RH_{1,2}$[a]	relative humidity		%
sh	surface height		cm
sh_{raw}	raw data of surface height		m
$solz$	solar zenith angle		degree
$solz_{slope}$	solar zenith angle for a slope		degree
$st_{1\text{-}6}$[b]	snow temperature		°C
$st\_depth_{1\text{-}6}$[b]	snow temperature sensor depth		m
SW_d	downward shortwave radiation		$W\,m^{-2}$
SW_{d_slope}	downward shortwave radiation for a slope		$W\,m^{-2}$
SW_{TOA}	downward shortwave radiation at the top of the atmosphere		$W\,m^{-2}$
SW_u	upward shortwave radiation		$W\,m^{-2}$
t_r	transmissivity of the atmosphere for shortwave radiation		no dimension
$T_{1,2}$[a]	air temperature		°C
$WD_{1,2}$[a]	wind direction		degree
$U_{1,2}$[a]	wind speed		$m\,s^{-1}$
α_{sw}	surface albedo		no dimension
$\alpha_{sw,i}$	daily integrated surface albedo		no dimension
α_{nir}	surface near-infrared albedo		no dimension
$\alpha_{nir,i}$	daily integrated surface near-infrared albedo		no dimension
β	slope angle		radian
ε_0	clear-sky atmospheric emissivity		no dimension
ε^*	atmospheric emissivity		no dimension
θ	solar zenith angle		radian
θ_{slope}	solar zenith angle for a slope		radian
ϕ	solar azimuth angle		radian
ϕ_{slope}	solar azimuth angle of a slope		radian

[a] 1: observed at lower height, 2: observed at upper height (only at the SIGMA-A site)

[b] 1-6: observing depth

103
104

3. Description of AWS systems and datasets

3.1. Specifications

Each AWS main mast is set in a hole drilled using a hand auger. Sensors for air temperature, relative humidity, and wind speed and direction are mounted at the ends of horizontal poles to exclude possible thermal and wind disturbances from the main mast. The SIGMA-A sensors are placed 3 m and 6 m above the surface, as signified by subscripts "1" (lower) and "2" (upper) in the corresponding data variables. The SIGMA-B sensors are set at 3 m above the surface and have subscripts of "1". The surface height sensor at both sites is mounted at 3 m height beneath the air temperature and relative humidity sensors. Six snow temperature sensors have been set as follows. Four sensors were set at 19:00 UTC on 29 June 2012 at depths of 100 cm (st_1), 70 cm (st_2), 40 cm (st_3), and 5 cm (st_4) under the snow surface. At 21:00 UTC on 27 July 2013, sensors st_3 and st_4 were relocated to depths of 46 cm and 16 cm, respectively. Sensors st_5 and st_6 were set at 5 cm under the surface and 45 cm above the surface, respectively, at 14:00 UTC on 9 June 2014. Sensors for shortwave, longwave, and near-infrared radiation are installed at SIGMA-A on separate poles 10 m from the main mast (Fig. 2a-2). A pyranometer and a pyrgeometer at SIGMA-B are mounted on the main mast facing directly south. Tilt angles of the main mast in the north-south ($Tilt_X$) and east-west ($Tilt_Y$) directions are monitored with an inclinometer attached to the main mast. The additional suffix "A" or "B" represents the site name in the variables introduced below.

Electric power is supplied to the AWS systems by a lead-acid battery that is charged constantly by solar panels attached to the main mast. All parameters are recorded once per minute and stored in a data logger (C-CR1000, Campbell Scientific, USA), except for the main mast's surface height and tilt angles, which are recorded every hour. Hourly data are calculated for the other parameters by averaging the 1-min data. All hourly data are sent regularly to the data server via the Argos satellite channel.

Surface height is measured with an ultrasonic snow gauge (Table 1). The raw data from this sensor (sh_{raw}) is the distance from the sensor to the snow surface, which has a temperature dependence. The temperature-corrected surface height (sh) is calculated from

$$sh = sh_{initial} - sh_{raw} \times \sqrt{\frac{T_2 + 273.15}{273.15}} \times 100, \qquad (i)$$

where $sh_{initial}$ (= 300 cm) is the initially installed sensor height from the surface and T_2 is air temperature.

3.2. Data processing

We describe the calculations for some variables used in the QC process in this section. To

138 accurately calculate the surface albedo and surface energy balance at the SIGMA-B site, we considered

139 the impact of the sloping surface on the vertical radiant flux. To account for this effect, we derived the

140 slope-corrected downward shortwave radiation (SW_{d_slope}) using the methods in Jonsell et al. (2003)

141 and Hock and Holmgren (2005). The SW_{d_slope} is calculated by

142 $$SW_{d\_slope} = I_s + I_d, \tag{ii}$$

143 where I_s and I_d are the direct and diffuse shortwave radiation for a slope, respectively:

144 $$I_s = SW_d \times d, \tag{iii}$$

145 $$I_d = SW_d \times (1 - d) \times \frac{\cos \theta_{slope}}{\cos \theta}, \tag{iv}$$

146 where d is the ratio of total diffuse radiation to global radiation and θ and θ_{slope} [radian] are the solar

147 zenith angle and the solar zenith angle for a slope, respectively. The ratio d is obtained from

148 atmospheric transmittance t_r by

149 $$d = \begin{cases} 0.15 & \text{for } 0.8 \leq t_r, \\ 0.929 + 1.134 t_r - 5.111 t_r{}^2 + 3.106 t_r{}^3 & \text{for } 0.15 < t_r < 0.8, \\ 1.0 & \text{for } t_r \leq 0.15, \end{cases} \tag{v}$$

150 where

151 $$t_r = \frac{SW_d}{SW_{TOA}}, \tag{vi}$$

152 where SW_{TOA} is the downward shortwave radiation at the top of the atmosphere, calculated by

153 $$SW_{TOA} = I_0 \left(\frac{r_m}{r}\right)^2 \cos \theta, \tag{vii}$$

154 where I_0 (= 1361 W m^{-2}) is the solar constant (Rottman, 2006; Fröhlich, 2012), r is the distance

155 between the Sun and the Earth (assuming an elliptical orbit with an eccentricity of 0.01637), and r_m is

156 its annual mean (= 1.496×10^8 km).

157 The solar zenith angle for a slope in Eq. (iv) is calculated by

158 $$\cos \theta_{slope} = \cos \beta \cos \theta + \sin \beta \sin \theta \cos(\varphi - \varphi_{slope}), \tag{viii}$$

159 where β is the slope angle from a horizontal plane, and φ and φ_{slope} are the solar azimuth and the solar

160 azimuth for the slope direction, respectively. Solar zenith and azimuth angles are calculated from the

161 geographic position of the observation site and the date and time.

162 Shortwave and near-infrared albedos (a_{sw} and a_{nir}, respectively) are calculated as the ratio of

163 upward and downward radiant fluxes, as shown for a_{sw} by

164 $$\alpha_{sw} = \frac{SW_u}{SW_d}, \tag{ix}$$

165 where SW_u is the upward shortwave radiant flux and SW_d is the downward shortwave radiant flux. The

166 daily integrated shortwave albedo ($a_{sw,i}$) is calculated as the ratio of cumulative upward and downward

167 radiant fluxes for the past 24 h:

168    $$\alpha_{\mathrm{sw,i}} = \sum_{24\mathrm{h}} SW_{\mathrm{u}} / \sum_{24\mathrm{h}} SW_{\mathrm{d}}. \tag{x}$$

169   The near-infrared albedo (a_{nir}) and daily integrated near-infrared albedo ($a_{\mathrm{nir,i}}$) are calculated in the

170   same way. The near-infrared fraction is the ratio of the downward near-infrared radiant flux (NIR_{d}) to

171   SW_{d}.

172   Note that some parameters may require correction or caution depending on the observation

173   environment. First, since temperature and humidity shelters are naturally ventilated, air temperature

174   value may have a positive bias due to shelter heating from solar radiation (e.g., Morino et al, 2021).

175   In addition, in sub-freezing conditions, relative humidity may not be measured correctly because the

176   sensor used in this study (Vaisala, HMP155) calculates relative humidity as liquid water vapor pressure

177   even in sub-freezing environments and if the shelter is covered by rime or frost (Makkonen and Laakso,

178   2005). Aoki et al. (2011) pointed out that the pole on which the radiometer is mounted casts a shadow

179   on the radiation sensor, which may result in incorrect radiation measurements. Although the possibility

180   of data correction as described above is recognized, the focus of this paper is to open the observed

181   values themselves, without any correction or data processing that might involve the implementer's

182   intention. Therefore, we will note only the correction possibilities and present the observed data in this

183   study.

184   **4. Quality control**

185   The datasets of observations at sites SIGMA-A and SIGMA-B are classified into four QC levels

186   numbered 1.0 to 1.3. A Level 1.0 dataset, which is not archived in any repository, is a raw dataset

187   without data processing. A Level 1.1 dataset is a raw dataset with flags added to indicate missing data

188   for periods when the data logger was inoperative. A Level 1.2 dataset has undergone an initial control,

189   which uses a simple masking algorithm to eliminate anomalous values that violate physical laws or

190   are impossible in the observed environment. The initial control improves the accuracy of the statistical

191   processing that follows and reduces the possibility of excluding true values. A Level 1.3 dataset has

192   undergone a secondary control, in which statistical methods are used on Level 1.2 data to identify and

193   mask outlier values. It has also undergone a final manual masking procedure, in which a researcher

194   visually checks the dataset and masks outliers based on subjective criteria.

195   The initial control method is described in Sect. 4.1 and the secondary control method is described

196   in Sect. 4.2. In these sections, the parameter suffixes related to the differences in observation height

197   (1 and 2) and sites (A and B) are omitted except when needed for clarity, and subscripts indicating

198   upward and downward radiation (d; downward, u; upward) is denoted as χ in the equation. Erroneous

199   records are flagged with one of the following numerical expressions to signify the reason they have

200   been flagged:

201   -9999: a missing or erroneous data record attributed to a mechanical malfunction or a local

202 phenomenon such as sensor icing, riming, or burial in snow.

203 −9998: an erroneous radiation record when the radiant sensor was covered with snow or frost.

204 −9997: a record of snow temperature sensor depth when the sensor was suspected to be located above,

205 not below the snow surface.

206 −8888: a record flagged during the manual masking procedure.

4.1. Initial QC for Level 1.2 datasets

208   The objectives of the initial control are to eliminate erroneous records due to mechanical
209 malfunctions or local phenomena and pre-treat Level 1.1 datasets for the secondary control. The initial
210 control consists of a range test (e.g., Fiebrich et al., 2010; Estévez et al., 2011) and a manual mask
211 procedure. The range test sets variation ranges (see Tables 3 and 4) for each observed parameter in
212 northwest Greenland on the basis of simple statistics (maximum, minimum, and mean values) derived
213 from records in the Level 1.1 dataset during a period with no obvious erroneous data. Records outside
214 this statistical range are flagged with a "−9999" code. Tables 3 and 4 list the parameters subjected to
215 this test and their assigned ranges. The manual masking procedure identified specific erroneous values
216 that resulted from an electrical malfunction and flagged them with a "−8888" code. The following
217 subsections offer detailed and additional explanations of the initial control, however, in the following
218 description, only the procedure numbers in Table 3 are referenced as necessary, and the explanation of
219 the range test is omitted.

4.1.1. Wind speed and wind direction

221   U_{max} used in the range test is the maximum value between the beginning of observation and 31
222 August 2020, and $+15.0$ m s^{-1} was taken as the range margin for the upper limit of U_n. In addition to
223 the range test, the following basic processing was also performed. When U_n was zero (no wind), WD_n
224 was flagged as erroneous:

225     $U_n = 0$ and $WD_n > 0 \rightarrow WD_n$ flagged −9999.   (1.1.1)

226 When WD_n had a negative value, it was flagged as erroneous:

227     $WD_n \leq 0 \rightarrow WD_n$ flagged −9999.   (1.1.2)

4.1.2. Air temperature and relative humidity

229   T_{n_max} and T_{n_min} were determined from the observation period ending 31 August 2020. The range
230 margin for T_n was set as ± 10.0 °C. Discrepancies arising from the dual sensors at SIGMA-A were
231 addressed in the secondary control (see Sect. 4.2.2).

4.1.3. Shortwave and near-infrared radiation

The main objective of the initial control for shortwave radiation was to mask erroneous records attributed to Zero Offset (Behrens, 2021). Zero Offset is a few watts of radiation that occurs at night caused by the slight temperature difference between the two detectors (inside of the dome shelter and sensor body). However, since the value is an observation error, the observed value may be different from the original radiation balance and need to be masked.

The range test is based on the assumption that SW_d cannot exceed the maximum of SW_{TOA} (SW_{TOA_max}) during the observation period (761.6 W m^{-2} at SIGMA-A and 772.2 W m^{-2} at SIGMA-B), and albedos a_{sw} and a_{nir} cannot be higher than a_{sw_max} and a_{nir_max} (a_{sw_max} = 0.95 and a_{nir_max} = 0.90), respectively, as determined from the radiative transfer model calculation (Aoki et al., 2003). Moreover, the fraction of the near-infrared spectral domain at the top of the atmosphere (f_{nir}) is assumed to be equal to 0.5151 based on the extraterrestrial spectral solar radiation (Wehrli, 1985). Based on those assumptions, upward and downward radiation fluxes were flagged as erroneous according to the range tests in Table 3.

The following procedures were also applied to mask erroneous records due to Zero Offset. These parameters were flagged as erroneous (-9999) in a following case (using SW_χ as an example):

$$SW_\chi < 0 \text{ and } solz < 90.0 \rightarrow SW_\chi \text{ flagged } -9999, \tag{1.3.1}$$

$$SW_\chi < 0 \text{ and } solz \geq 90.0 \rightarrow SW_\chi = 0. \tag{1.3.2}$$

4.1.4. Longwave radiation

The range tests were performed for LW_d and LW_u under the conditions in Table 3. LW_{d_max} and LW_{u_max} were determined as follows:

$$LW_{d\_max} = \varepsilon_{max} \sigma\, T_{max}, \tag{1.4.1}$$

$$LW_{u\_max} = \varepsilon \sigma\, T_{s\_max}. \tag{1.4.2}$$

However, T_{max} is T_{2A_max} for the SIGMA-A site and T_{1B_max} for the SIGMA-B site. Maximum values were determined under the following assumptions: (1) T_{2A} and T_{1B} cannot be larger than T_{2A_max} and T_{1B_max}, respectively, (2) atmospheric emissivity is set to unity (ε_{max}), and (3) the value of LW_{u_max} is determined as the amount of radiation corresponding to longwave emission at T_{s_max} (= 10 °C), which includes errors due to longwave emissions from the poles of the AWS system and similar sources, and that the emissivity of the snow/ice surface (ε) is 0.98 (Armstrong and Brun, 2008).

Both upward and downward longwave fluxes were considered erroneous when the sensor appeared to be covered with snow or frost:

$$|LW_d - LW_u| \leq 1.0 \rightarrow LW_d \text{ and } LW_u \text{ flagged } -9998. \tag{1.4.3}$$

4.1.5. Surface height

The range test for surface height (*sh*) was imposed separately for each period between maintenances to the SIGMA-A site, when the main mast extension was adjusted to prevent the sensors from being buried in snow. (A single range test sufficed for SIGMA-B.) For each test, the range was set so that *sh* varied from the median by ±100 cm or ±150 cm, a margin that was determined depending on the variation of the data records in each period. The objective of this range test (Procedure 1.5.1; Table 3) was to mask the most obvious outliers. In addition, corrections were made to the *sh* records after each of three maintenance visits to the AWS at SIGMA-A.

4.1.6. Atmospheric pressure

P_{a_ave} used in the range test is the average atmospheric pressure for the observation period at each AWS site (Table 3). The additional margin that defined the range was ±100 hPa.

4.1.7. Snow temperature

The range test for snow temperature was conducted using following threshold values; T_{1_min} is the minimum air temperature for the site and the upper threshold, 0.2 °C, incorporates the sensor's absolute error of 0.15 °C and the requirement that the snow temperature cannot be positive.

Table 3. Range test coverage for each parameter used in the QC procedures. The variable subscripts "n" (1 or 2) and χ indicate the distinction of sensors height and the direction of radiation flux (upward or downward), respectively.

parameter	variable	unit	range test	procerdure No.
			value range	
wind speed	U_1, U_2	m s^{-1}	$0 < U_n < U_{max} + 15.0$	1.1.3
wind direction[a]	WD_1, WD_2	degree	$0 < WD_n \leqq 360$	1.1.4
air temperature	T_1, T_2	°C	$T_{n\_min} - 10.0 < T_n < T_{n\_max} + 10.0$	1.2.1
relative humidity	RH_1, RH_2	%	$0 \leqq RH_n \leqq 100$	1.2.2
shortwave radiation	SW_d, SW_u	W m^{-2}	$SW_d < SW_{TOA\_max}$	1.3.3
			$SW_u < SW_{TOA\_max} \times a_{sw\_max}$	1.3.5
			$SW_d < T_{rA\,(or\,B)} \times SW_{TOA\_max}$	2.3.2
near-infrared radiation[b]	NIR_d, NIR_u	W m^{-2}	$NIR_d < f_{nir} \times SW_{TOA\_max}$	1.3.4
			$NIR_u < f_{nir} \times SW_{TOA\_max} \times a_{nir\_max}$	1.3.6
			$NIR_d < T_{rA} \times f_{nir} \times SW_{TOA\_max}$	2.3.3
surface albedo	a_{sw}	–	$0.6 < a_{sw} < 0.95$ (for October–April in SIGMA-A)	2.4.1
			$0.4 < a_{sw} < 0.95$ (for May–September in SIGMA-A)	2.4.2
			$0.4 < a_{sw} < 0.95$ (for October–April in SIGMA-B)	2.4.3
			$0.1 < a_{sw} < 0.95$ (for May–September in SIGMA-B)	2.4.4
surface near-infrared albedo	a_{nir}	–	$0.5 < a_{nir} < 0.90$ (for October–April in SIGMA-A)	2.4.5
			$0.3 < a_{nir} < 0.90$ (for May–September in SIGMA-A)	2.4.6
longwave radiation	LW_d, LW_u	W m^{-2}	$0 < LW_\chi < LW_{\chi\_max}$	1.4.4
surface height	sh	cm	median_sh $- 100.0$ or $150.0^c < sh <$ median_sh $+ 100.0$ or 150.0^c	1.5.1
atmospheric pressure	P_a	hPa	$P_{a\_ave} - 100.0 < P_a < P_{a\_ave} + 100.0$	1.6.1
snow temperature[b]	st	°C	$T_{1\_min} - 10.0 < st_n < 0.2$	1.7.1

[a] in case of $U_n > 0$
[b] only SIGMA-A site
[c] the margin is changed depending on a variation of the data record in each applied period.

284

285 Table 4. Threshold values used in the range tests, determined from the entire observation period up to

286 31 August 2020.

meteorological parameter	unit	threshold value			
		SIGMA-A		SIGMA-B	
		parameter name	value	parameter name	value
wind speed	m s^{-1}	U_{1A_max}	23.9	U_{1B_max}	21.9
		U_{2A_max}	25.5	−	−
air temperature	°C	T_{1A_max}	7.2	T_{1B_max}	10.7
		T_{2A_max}	7.2	−	−
		T_{1A_min}	−49.9	T_{1B_min}	−40.5
		T_{2A_min}	−49.9	−	−
longwave radiation	W m^{-2}	LW_{dA_max}	418.8	LW_{dB_max}	440.1
		LW_{uA_max}	357.2	LW_{uB_max}	357.2
atmospheric pressure	hPa	P_{a_aveA}	833.1	P_{a_aveB}	894.2

287

288

4.2. Secondary QC for Level 1.3 datasets

290 The secondary control applies another range test, an anomaly test, and a manual mask procedure.

291 The range test sets a more precise variation range than the initial control and masks erroneous data

292 records. The anomaly test sets a median and standard deviation (SD), which govern statistical tests as

293 follows;

294 $$\beta < \text{median}\_\beta + \text{SD}\_\beta \times \gamma,$$ (2.0.1)

295 where β is an arbitrary variable and the multiplier γ is 1, 2, or 3 depending on the intensity of the

296 anomaly variation, and determined based on the test results in each case. This study determined the

297 possible range of normal values in the Level 1.2 dataset and identify and mask outliers if the variable

298 deviates from its normal range. The manual mask procedure identifies and masks any remaining

299 erroneous records. As a result of data masking by the initial control and the secondary control, the

300 percentage of unmasked records for each parameter at three data levels is shown in Table 5, and the

301 effects of the two controls are illustrated in Fig. 3 and described in detail below.

302

303 Table 5. Percentage of unmasked data for each parameter in each dataset.

	SIGMA-A			SIGMA-B		
	Level 1.1	Level 1.2	Level 1.3	Level 1.1	Level 1.2	Level 1.3
	%	%	%	%	%	%
U_1	98.0	98.0	92.1	99.7	99.7	97.7
WD_1	98.0	96.7	91.8	99.7	99.2	97.2
T_1	98.0	73.4	68.4	99.7	99.7	99.7
RH_1	98.0	50.7	43.6	99.7	99.7	98.8
U_2	98.0	98.0	94.1	–	–	–
WD_2	98.0	97.1	93.8	–	–	–
T_2	98.0	98.0	97.8	–	–	–
RH_2	98.0	98.0	98.0	–	–	–
SW_d	98.0	97.9	86.2	99.7	99.5	85.2
SW_u	98.0	97.9	98.1	99.7	99.7	99.7
LW_d	98.0	75.3	68.9	99.7	91.0	91.0
LW_u	98.0	68.7	67.4	99.7	91.0	91.0
NIR_d	98.0	97.9	86.6	–	–	–
NIR_u	98.0	97.9	98.0	–	–	–
sh	98.0	85.5	75.8	99.7	90.2	87.1
P_a	98.0	97.9	97.9	99.7	99.7	99.7
st_1	98.0	97.6	96.7	–	–	–
st_2	98.0	97.9	97.3	–	–	–
st_3	98.0	88.8	87.2	–	–	–
st_4	98.0	97.0	96.2	–	–	–
st_5	98.0	94.9	72.3	–	–	–
st_6	98.0	95.2	56.7	–	–	–
a_{sw}	–	–	31.6	–	–	32.4
a_{nir}	–	–	33.5	–	–	–
st_depth_1	–	–	75.8	–	–	–
st_depth_2	–	–	75.8	–	–	–
st_depth_3	–	–	75.8	–	–	–
st_depth_4	–	–	75.8	–	–	–
st_depth_5	–	–	52.7	–	–	–
st_depth_6	–	–	36.9	–	–	–
SW_{d_slope}	–	–	–	–	–	83.7

304
305

306
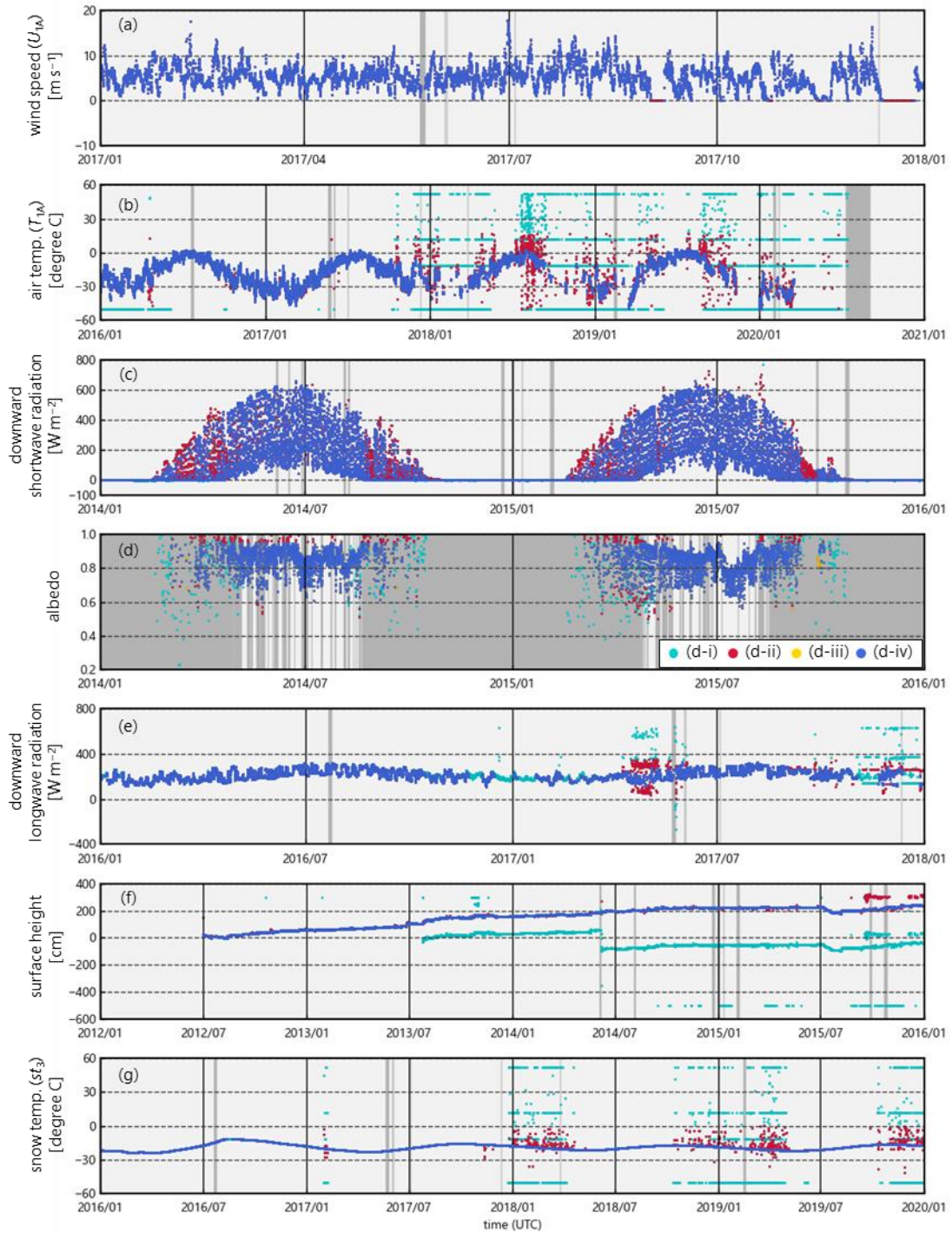
Figure 3. Examples of the initial and secondary controls for the SIGMA-A site: (a) wind speed (U_{1A}),
(b) air temperature (T_{1A}), (c) downward shortwave radiation, (d) surface albedo, (e) downward
longwave radiation, (f) surface height, and (g) snow temperature (st_3). In all panels except (d), the dark
gray areas represent time periods in which data records in the Level 1.0 dataset were masked to
produce the Level 1.1 dataset, light blue dots denote records masked by the initial control, red dots

312   denote records masked by the secondary control, and dark blue dots are the Level 1.3 data records. In
313   panel (d), the gray shaded area represents the masked (−9999) data records that cannot be calculated
314   due to the absence of, masked SW_d, or for other reasons. The light blue, red and yellow dots represent
315   data points masked by three QC operations during the secondary control; see Sect. 4.2.4 for
316   explanation.

4.2.1. Wind speed and wind direction

318   When U_n was zero for more than 6 continuous hours, U_n and WD_n were both flagged as erroneous
319   (−9999) under the assumption that the wind sensor was blocked by snow and ice. Although the initial
320   control eliminated no U_n records, this step masked many values in the winter (Fig. 3a).

4.2.2. Air temperature and relative humidity

322   Anomaly tests for air temperature and relative humidity were only applied to the lower-level
323   sensor records for SIGMA-A (i.e., T_{1A} and RH_{1A}). The anomaly test compared the difference (ΔT and
324   ΔRH) between readings of the upper and lower sensors (i.e., $|T_{1A} - T_{2A}|$ and $|RH_{1A} - RH_{2A}|$) to the
325   respective medians and SDs of those parameters. The medians were calculated from the data before 1
326   September 2017, because the data after that date appeared to include many erroneous T_{1A} records due
327   to deterioration of the data logger or sensor. The SD criterion (γ in Procedure 2.0.1) was adjusted
328   modestly ($\gamma = 3$) before 1 September, 2017 and more stringently ($\gamma = 1$) to detect outliers in the records
329   of T_{1A} and RH_{1A} after the date, which were flagged as erroneous (−9999). The effectiveness of this
330   adjustment is clear in Fig. 3b.

4.2.3. Shortwave and near-infrared radiation

332   The anomaly test for shortwave and near-infrared radiation was intended to mask the noise
333   resulting from a weak electric pulse at large solar zenith angles. The median and SD values were
334   calculated from only the records (SW_d, SW_u, NIR_d, and NIR_u) at $solz > 90.0°$ to distinguish this noise
335   source according to Procedure 2.0.1 for above parameters, where $\gamma = 3$. If the record deviates from its
336   anomaly range, the records were identified as noise and modified to zero.
337   The downward radiation components were sometimes overestimated as a result of icing or riming
338   over the glass dome of the pyranometer. To mask these erroneous values, we applied range tests based
339   on SW_{TOA} and threshold values of atmospheric transmittance for each site T_{rA} and T_{rB} ($T_{rA} = 0.881$
340   and $T_{rB} = 0.872$) calculated by a radiative transfer model (Aoki et al., 1999, 2003) shown in Table 3.
341   Values of SW_d and NIR_d that were outside the range were flagged as erroneous (−9999).
342   To recognize other instances when the radiation sensor was covered with snow or frost, SW_d and
343   NIR_d records corresponding to the following case that downward radiation is smaller than upward

344   radiation was flagged as erroneous (−9998), using SW_χ as an example:

345        $SW_d < SW_u$.   (2.3.1)

346   Figure 3c shows that the initial control eliminated a few erroneous SW_d data recorded in August 2015,

347   whereas the secondary control masked many records, especially in February–May, that were affected

348   by riming or frost.

349   **4.2.4. Shortwave and near-infrared albedo**

350   We calculated albedos a_{sw} and a_{nir} from the SW_d and NIR_d datasets that were completed the

351   secondary control. This calculation was done in four separate steps, shown by the color of dots in Fig.

352   3d.

353   (1) Flagging for low pyranometer sensitivity

354   At solar zenith angles near 90.0°, SW_d and NIR_d may not be an accurate measurement because of

355   the low sensitivity of the pyranometer. We therefore masked a_{sw} and a_{nir} values at $solz > 85.0°$ or when

356   the SW_d (NIR_d) value was below the median SW_d (NIR_d) value for $solz > 85.0°$. Records masked in this

357   step are shown in Fig. 3d as light blue dots (d-i).

358   (2) Range test for cold and warm periods

359   The range test used the upper and lower thresholds for a_{sw} and a_{nir} shown in Table 3, as determined

360   by the radiative transfer calculation of Aoki et al. (2003, 2011) plus a small error margin. Those

361   thresholds correspond to the assumed surface conditions during two parts of the year. For the cold

362   period of October–April, we used the lower thresholds for dry snow at the SIGMA-A site and dry or

363   wet snow at the SIGMA-B site conditions. For the warm period of May–September we used the

364   thresholds for wet snow at the SIGMA-A site and wet snow or dark ice at the SIGMA-B site conditions.

365   Records with albedo values beyond these theoretical thresholds were masked.

366   (3) Anomaly test in low atmospheric transmittance condition

367   The range test was augmented by an anomaly test to identify underestimates of a_{sw} and a_{nir} when

368   SW_d (NIR_d) was low and atmospheric transmittance (t_r) was small, typically at large solar zenith angles.

369   We masked a_{sw} (a_{nir}) values that were unnaturally low owing to low t_r and SW_d (NIR_d) in $solz > 80.0°$

370   condition. Data records that were masked in either the range or anomaly tests are shown in Fig. 3d as

371   red dots (d-ii).

372   (4) Final steps

373   In cases where LW_d was flagged as "−9998" during the initial control (see Sect. 4.1.4), a_{sw} and a_{nir}

374   were flagged as "−9999" under the assumption that the radiation sensors were covered with snow or

375   frost. The final step was a manual mask procedure. Data records that were masked in this phase are

376   shown in Fig. 3d as orange dots (d-iii), and the final Level 1.3 dataset is displayed as blue dots (d-iv).

4.2.5. Longwave radiation

The anomaly test for LW_d and LW_u was conducted only for the SIGMA-A dataset using a standard longwave radiant flux (LW_{std}), a measure of the amount of longwave radiation from the near-surface atmosphere that was calculated from the air temperature measurement by Brock and Arnold (2000)

$$LW_{std} = \varepsilon^* \sigma (T_{2A} + 273.15)^4, \qquad (xi)$$

$$\varepsilon^* = (1 + \kappa n)\varepsilon_0, \qquad (xii)$$

$$\varepsilon_0 = 8.733 \times 10^{-3} \times (T_{2A} + 273.15)^{0.788}, \qquad (xiii)$$

where ε^* is the atmospheric emissivity, σ (= 5.670×10^{-8}) is the Stefan–Boltzmann constant, κ (= 0.26) is a constant depending on cloud type (Braithwaite and Olsen, 1990), n is the cloud cover amount (n: [0, 1] and set at 0.5 because it could not be determined), and ε_0 is the clear-sky emissivity. We assumed that LW_{std} was a close approximation of the true longwave radiant fluxes and used the absolute difference between LW_{std} and LW_d or LW_u (i.e., ΔLW_d or ΔLW_u) and its median and SD as the basis of the anomaly test as following Procedure 2.0.1.

Because parts of the LW_d dataset contained many erroneous records attributed to degradation of the data logger (see Fig. 3e), we reduced the SD criterion ($\gamma = 1$) in 7 April to 7 June 2017 and after 1 September 2017. Except for those two periods, γ was set to "2" for both ΔLW_d and ΔLW_u. LW_d and LW_u records that were outliers under the criteria were flagged as erroneous (-9999). Figure 3e shows that the initial control (see Sect. 4.1.4) improved this anomaly test's efficacy, and the secondary control yielded a clean LW_d time series.

4.2.6. Surface height

The anomaly test for surface height masked data that displayed unrealistic fluctuations. Differences (Δsh) were determined with respect to mean and SD values from the preceding 72 h values during period 1, before 1 September 2017 (sh_{mean1}) and period 2, after 1 September 2017 (sh_{mean2}). The Δsh values were compared to the median plus SD of Δsh for that period. In the period 1, the SD criterion in Procedure 2.0.1 was strict ($\gamma = 1$), and in the period 2, the criterion was relaxed ($\gamma = 3$). In addition, because surface height increased steadily in period 2, we derived the regression equation for this increase and identified outliers with respect to the SD of the regression, i.e. Δsh_{reg} as follows:

$$\Delta sh_{reg} < SD_{reg\_}sh \qquad \text{for after 1 September 2017.} \qquad (2.6.1)$$

Records of sh that varied beyond the anomaly ranges were flagged as erroneous (-9999).

A manual mask procedure was added as a final step. The result of QC procedure is shown in Fig. 3f. The initial control, which corrected gaps resulting from the AWS maintenance (see Sect. 4.1.5), yielded the smoothed data record that enabled the application of the anomaly test. Sensor height dataset was made using initial sensor height (3 or 6 m) and the QC completed temporal surface height data. Therefore, QC for sensor height data has already been implemented through the QC for surface height

411   data.

4.2.7. Snow temperature

413   In the first step, data records were masked when the snow temperature sensor was suspected to be
414   located above the snow surface:

415        $st\_depth_n < -1.0 \rightarrow st_n$ flagged -9999.   (2.7.1)

416   where st_depth_n was calculated using surface height data and the initial setting depth of sensor "n"
417   (see Sect. 3). The threshold of st_depth_n included a margin of 1.0 cm to reflect the accuracy of the
418   surface height sensor. The st_n was flagged as "-9997" if we could not judge whether the snow
419   temperature sensor was located below the snow surface.

420   The anomaly test for st_n consisted of two procedures. The first procedure relied on a temperature
421   gap (Δst_{d1}) between st_4 and data from each of the other five levels (st_{not4}) (i.e., $\Delta st_{d1} = |st_4 - st_{not4}|$),
422   because st_4 had very few erroneous data. The SD criterion (γ) for this anomaly test was changed for
423   each parameter depending on the variability of the data. The second procedure used the difference
424   (Δst_{d2}) between st_n and its mean value st_{n_mean} from the previous 72 h ($\Delta st_{d2} = |st_n - st_{n\_mean}|$),
425   calculated using the same method as sh_{mean} (see Sect. 4.2.6). The SD criteria (γ) were all unity in this
426   test. In both procedures, the median and SD terms were calculated from records for the full time period.
427   Records detected as outliers were flagged as "-9999". Figure 3g shows the results of all procedures,
428   using st_3 as an example.

4.2.8. Atmospheric pressure

430   The time series of P_a included only a few erroneous records. We masked outliers on the basis of

431        $|P_a - P_{a\_mean}| > 20.0$,   (2.8.1)

432   where P_{a_mean} is the average for the past 3 h (excluding masked data records). We set the threshold at
433   20.0, a higher value than the SD, because using the SD could have masked valid records.

5. Temporal variations of meteorological parameters

435   This section shows the results of simple analyses of the Level 1.3 dataset.

5.1. Air temperature and surface height

437   Figure 4 shows the air temperature fluctuations and surface height (*sh)* variations at both sites.
438   Mean air temperatures (2013–2019) were −18.1 °C at the SIGMA-A site and −12.3 °C at the SIGMA-
439   B site. The annual maxima were recorded every July at both sites, except for August 2019 at the
440   SIGMA-B site. In contrast, the annual minima occurred in different months between December and

441 March. The maximum was slightly positive at the SIGMA-A site, and it was above freezing in all

442 years at the SIGMA-B site. Unusually high temperatures were recorded in mid-July 2015 (7.2 °C at

443 SIGMA-A and 10.7 °C at SIGMA-B). Air temperatures exceeding 5.0 °C at SIGMA-A and 10.0 °C at

444 SIGMA-B were common during that period.

445 Surface height steadily increased at the SIGMA-A site during the 8-year study period (Fig. 4), in

446 which sh rose approximately 1 m in the mass-balance years (September to August) of 2013/14,

447 2016/17, and 2017/18, and decreased slightly in the summers of 2011/12, 2014/15, and 2019/20.

448 Accumulations were notable in autumn and relatively small in winter. At the SIGMA-B site, in contrast,

449 increases and decreases in sh were observed during each mass-balance year. Decreases in sh during

450 summers were rare during the summers of 2012/13 and 2017/18 but common during the 2013/14,

451 2014/15, 2015/16, 2018/19, and 2019/20 summers, when decreases were greater than 1 m.

452
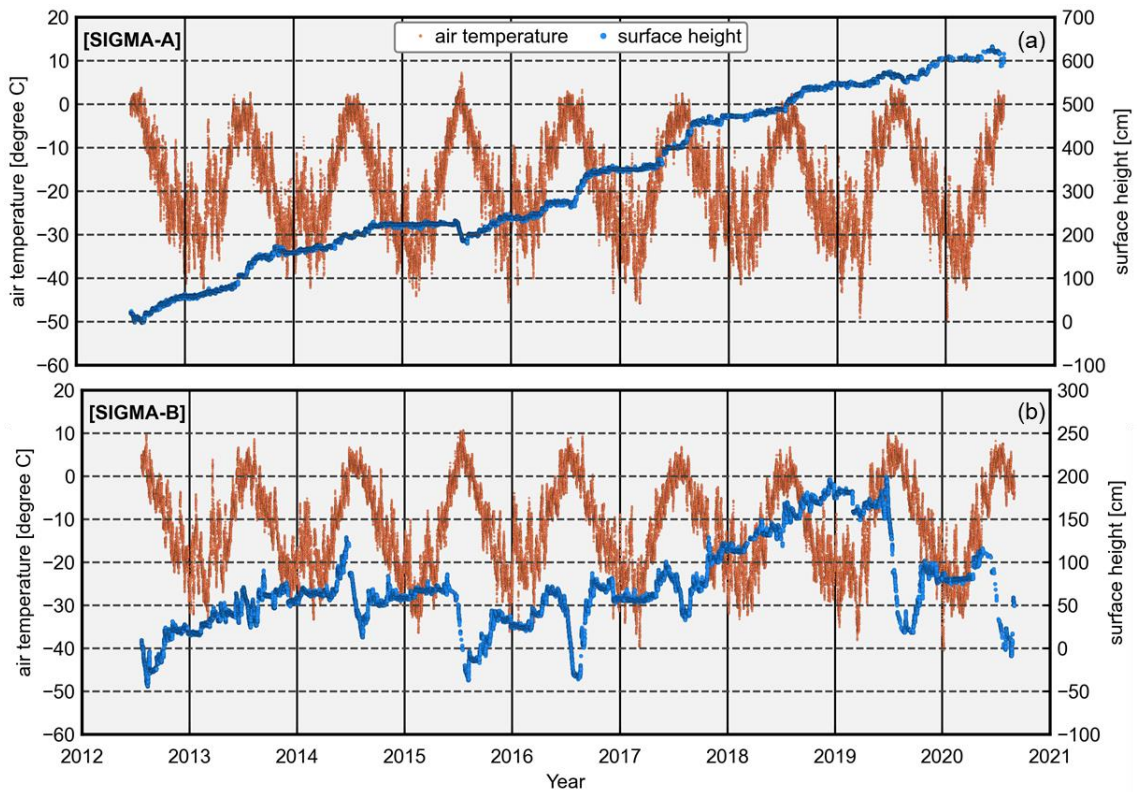
453

454 Figure 4. Time series of hourly air temperature and surface height at the (a) SIGMA-A (showing T_2

455 data) and (b) SIGMA-B sites.

456

457 **5.2. Atmospheric pressure and seasonal variation of temperature lapse rate**

458 The time series of atmospheric pressure (P_a) at the SIGMA-A and SIGMA-B sites show a clear

459 seasonal variation, high in summer and low in winter (Fig. 6). The two data records had similar

460   variation patterns that were strongly correlated ($r = 0.98$). The mean values for the whole observation
461   period were 833.1 hPa at site SIGMA-A and 894.2 hPa at site SIGMA-B (Table 4). The difference in
462   monthly mean P_a between the sites was smaller in summer and larger in winter (Fig. 7a), and the
463   amplitude of the annual cycle was greater at the SIGMA-A site.

464
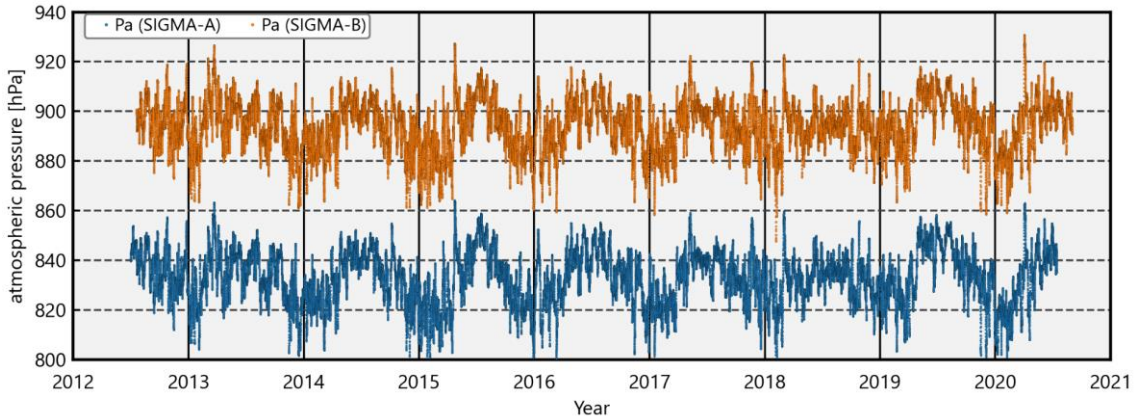
465
466   Figure 6. Time series of hourly atmospheric pressure (P_a) at the SIGMA-A and SIGMA-B sites.

467

468
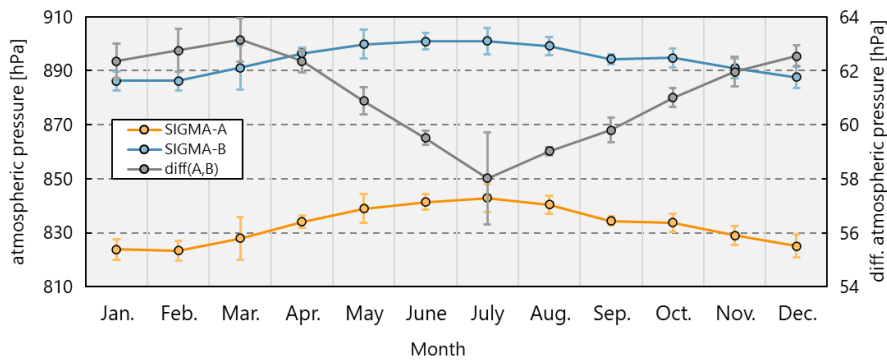
469
470   Figure 7. Time series of ensemble averages of monthly mean atmospheric pressures during all years
471   at both sites and their difference. Error bars indicate ±1 SD.

472

473   **5.3. Albedo**

474   Whereas shortwave albedo (a_{sw}) was rarely lower than 0.7 at site SIGMA-A, near-infrared albedo
475   (a_{nir}) was below 0.6 in 2012, 2015, 2016, 2019, and 2020 (Fig. 8). Because a_{nir} depends on the snow
476   grain size (Wiscombe and Warren, 1980), this finding implies that snow metamorphism progressed at
477   the SIGMA-A site in those years (Hirose et al., 2021). A strong decrease in a_{sw} was observed at the
478   SIGMA-B site during those same summers, which corresponded to notable decreases in surface height
479   (Fig. 4b) and high PDDs (Fig. 5). The decreases in albedo may have accelerated snowmelt and caused

480 the decreases in surface height at SIGMA-B during the warm summers of those years (see Sect. 5.1).
481 It appears that the difference in albedo reduction between the SIGMA-A and SIGMA-B sites in
482 summer originated from the difference in air temperature between the sites.

483
484
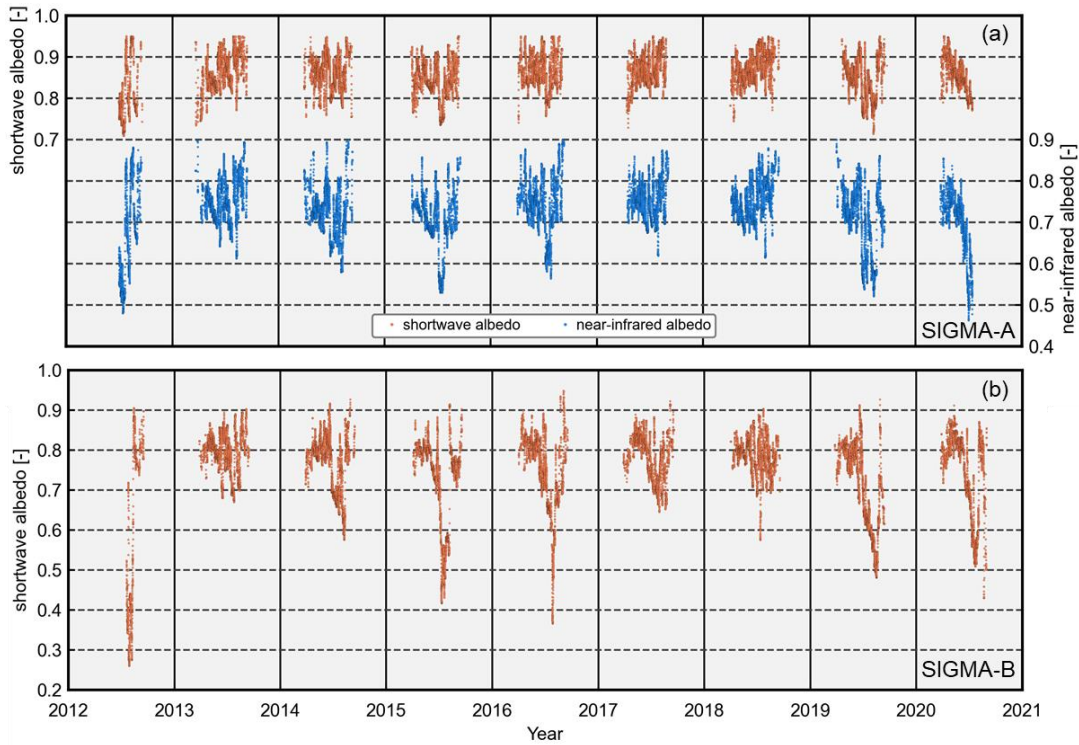
485
486 Figure 8. Time series of hourly shortwave and near-infrared albedos at the (a) SIGMA-A and (b)
487 SIGMA-B sites.

488

489 **5.4. Snow temperature**

490   Figure 9 shows the time series of snow temperatures (st_1–st_6) and snow sensor depths (st_depth_{1-}
491 $_6$). The sensor depths were calculated from each sensor's initial depths (see Sect. 3.1) and the surface
492 height variations at the SIGMA-A site. Seasonal and short-term snow temperature fluctuations were
493 observed, which became smaller after the 2016/17 winter season, when snow accumulation was very
494 large (Fig. 4). We assumed that the sensors were buried more deeply at that time, resulting in smaller
495 fluctuations in snow temperature. The annual mean snow temperatures after 2016, a year in which
496 snow temperatures were relatively stable and less variable, were between -18.9 ± 0.5 °C (st_4) and
497 -19.5 ± 1.7 °C (st_5).
498   Sensors recorded relatively high snow temperatures when they were positioned at shallow depths
499 below the snow surface. However, in the summer of 2015, sensors st_3 and st_4 registered 0 °C even

500   though they were more than 1 m below the snow surface. Air temperatures above freezing, and a large

501   decrease in surface height were observed in this period (Figs. 4 and 5); thus, it is plausible that

502   snowmelt occurred from the surface to depths near 120 cm, where st_3 was located at that time.

503
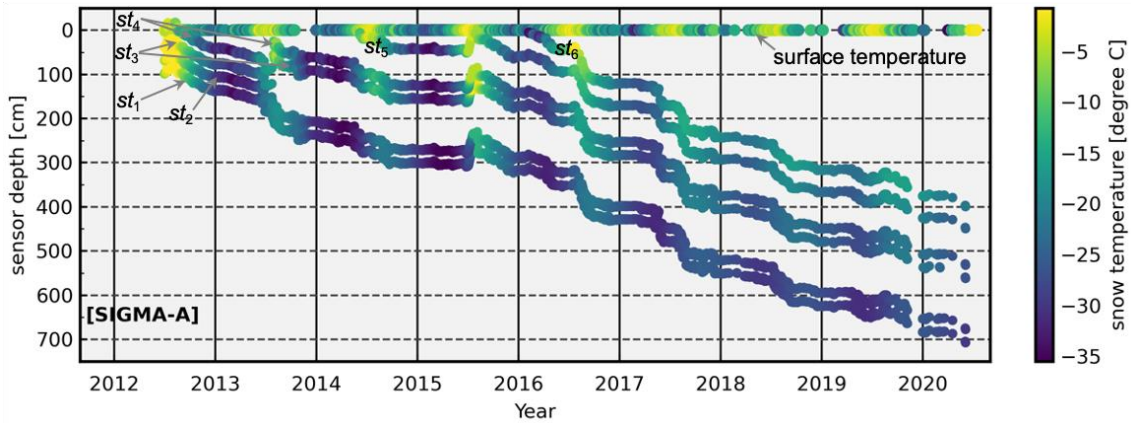
504

505   Figure 9. Time series of hourly snow temperatures (st_1–st_6), sensor depth, and surface temperature

506   (calculated from upward longwave radiation) at the SIGMA-A site.

507

508   **5.5. Longwave radiation**

509   The occurrence frequency of longwave radiation, taken to represent the atmospheric condition, is

510   often used as an indicator of climatological cloudiness (Stramler et al., 2011). Figure 10 shows the

511   histograms of occurrence frequency of downward (LW_d) and net longwave radiation ($LW_{net} = LW_d -$

512   LW_u) during July of all years at the SIGMA-A and SIGMA-B sites. The corresponding histograms for

513   the four seasons (autumn: SON, winter: DJF, spring: MAM, summer: JJA) are shown in Figs. S1 and

514   S2. The July LW_d data from both sites had bimodal distributions, with a lower mode of 220–240 W

515   m^{-2} at SIGMA-A and 240–260 W m^{-2} at SIGMA-B, and a higher mode of 290–310 W m^{-2} at SIGMA-

516   A and 310–330 W m^{-2} at SIGMA-B. The histograms of July and seasonal LW_{net} had similar but clearer

517   bimodal distributions, with modes at approximately 0 W m^{-2} and −70 W m^{-2} (Figs. 10c-d and S2).

518   LW_{net} can be regarded as an indicator of cloudiness, which can significantly change the downward

519   longwave radiation and thus the surface temperature of the snow or ice. Both downward and net

520   longwave radiation increase under overcast conditions because of blackbody radiation from the cloud

521   cover that is absent in clear-sky conditions. Stramler et al. (2011) and Morrison et al. (2012) have

522   argued that surface net longwave radiative flux has two modes in occurrence frequency (at −40 W m^{-2}

523   and 0 W m^{-2}), which correspond to clear-sky and overcast (low-level mixed-phase clouds) conditions.

524   In overcast conditions, because the cloud base and the surface are in thermal equilibrium, the vertical

525   thermal gradient is small and the longwave radiation budget is balanced ($LW_{net} = 0$ W m^{-2}) at the

526   surface. The two modes of LW_{net} (0 W m^{-2} and −70 W m^{-2}) at the two AWS sites appear to correspond

527 to the modes proposed by these earlier studies.

528 The occurrence frequency of LW_{net} in JJA appears to be more variable than those for the other

529 seasons at both sites (Fig. S2). In these months, the air temperature rises and sea ice extent decreases,

530 increasing the water vapor supply and advection from the surrounding sea to coastal Greenland (Kim

531 and Kim, 2017; Liang et al., 2022). In such atmospheric conditions, the cloud formation process is

532 susceptible to synoptic-scale disturbances. The histogram of LW_{net} for July (Fig. 10) indicates clear-

533 sky ($LW_{net} \cong -70$ W m^{-2}) in 2015, 2019, and 2020 and overcast conditions ($LW_{net} \cong 0$ W m^{-2}) in 2014

534 and 2018. In contrast, annual occurrence frequencies for SON and MAM were less variable than those

535 for JJA. Overcast and clear-sky conditions dominated in SON and MAM, respectively. Our analysis

536 shows that cloudiness in JJA was more variable than in other seasons, a result that is also borne out by

537 satellite observations (Ryan et al., 2022).

538
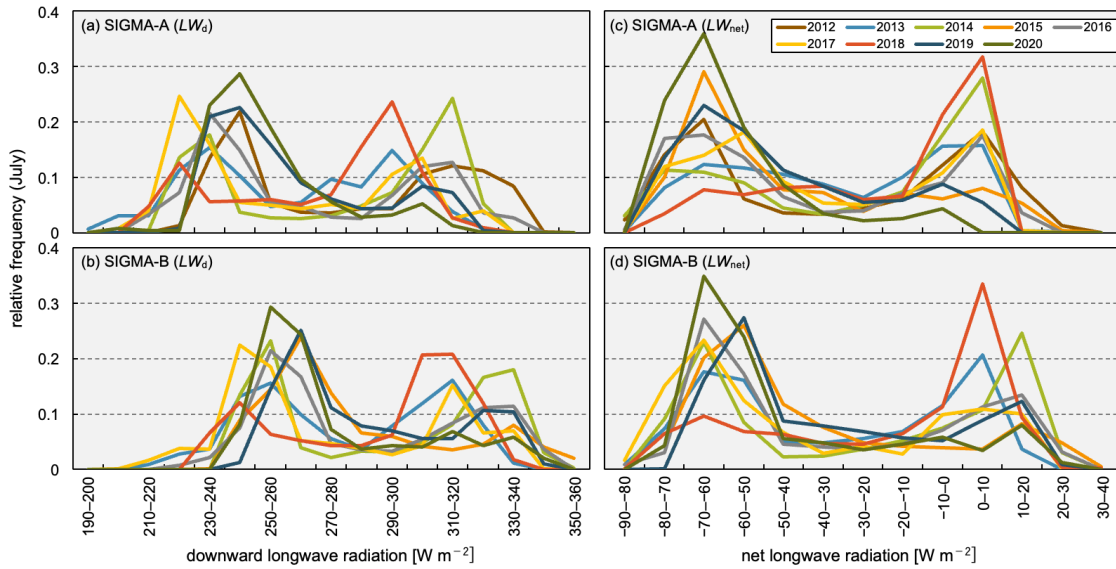
539

540 Figure 10. Histograms of the occurrence frequency of hourly downward longwave radiation (LW_d) and

541 net longwave radiation (LW_{net}) observed at the SIGMA-A and SIGMA-B sites in July of all years in

542 the study period. Each relative frequency represents the fraction of the total contained in each 10 W

543 m^{-2} bin.

544 **6. Data availability**

545 The Level 1.1, 1.2, and 1.3 datasets from this study are archived and available from the Arctic Data

546 archive System (ADS) in the National Institute of Polar Research (Table 6), where they are stored in

547 text (CSV) file format. Detailed information on the data content is presented in the file

548 "data_format_*site-name_data-level*.csv" associated with each of these dataset files.

549

550 Table 6. Information for the archived datasets from the SIGMA-A and SIGMA-B sites.

SIGMA-A	
Level 1.1	
data name:	Quality-controlled datasets of Automatic Weather Station (AWS) at SIGMA-A site from 2012 to 2020: Level: 1.1
file name:	SIGMA_AWS_SiteA_2012-2020_Lv1_1.csv
citation:	http://doi.org/10.17592/001.2022041301
reference:	Nishimura et al. (2023a)
Level 1.2	
data name:	Quality-controlled datasets of Automatic Weather Station (AWS) at SIGMA-A site from 2012 to 2020: Level: 1.2
file name:	SIGMA_AWS_SiteA_2012-2020_Lv1_2.csv
citation:	http://doi.org/10.17592/001.2022041302
reference:	Nishimura et al. (2023b)
Level 1.3	
data name:	Quality-controlled datasets of Automatic Weather Station (AWS) at SIGMA-A site from 2012 to 2020: Level: 1.3
file name:	SIGMA_AWS_SiteA_2012-2020_Lv1_3.csv
citation:	http://doi.org/10.17592/001.2022041303
reference:	Nishimura et al. (2023c)
SIGMA-B	
Level 1.1	
data name:	Quality-controlled datasets of Automatic Weather Station (AWS) at SIGMA-B site from 2012 to 2020: Level 1.1
file name:	SIGMA_AWS_SiteB_2012-2020_Lv1_1.csv
citation:	http://doi.org/10.17592/001.2022041304
reference:	Nishimura et al. (2023d)
Level 1.2	
data name:	Quality-controlled datasets of Automatic Weather Station (AWS) at SIGMA-B site from 2012 to 2020: Level 1.2
file name:	SIGMA_AWS_SiteB_2012-2020_Lv1_2.csv
citation:	http://doi.org/10.17592/001.2022041305
reference:	Nishimura et al. (2023e)
Level 1.3	
data name:	Quality-controlled datasets of Automatic Weather Station (AWS) at SIGMA-B site from 2012 to 2020: Level 1.3
file name:	SIGMA_AWS_SiteB_2012-2020_Lv1_3.csv
citation:	http://doi.org/10.17592/001.2022041306
reference:	Nishimura et al. (2023f)

551

7. Summary and conclusion

553   This paper describes the in situ meteorological datasets from the SIGMA-A and SIGMA-B AWS
554 sites in northwest Greenland and details the QC methods used in preparing the datasets. At this time
555 when drastic environmental change is proceeding in the Arctic region, sound meteorological data and
556 QC methods are of ever-growing importance.

557   The QC method offered here consists of two basic steps. The first step, the initial control, masks
558 observations that are affected by mechanical malfunctions or local phenomena and is a pre-treatment
559 for the second QC step. This step uses simple statistics to set the range of permissible variation in
560 northwest Greenland for each observational parameter and flags erroneous records on the basis of that

561 variation range. The second QC step, the secondary control, masks erroneous observations based on
562 more stringent variation ranges as determined by the median and SD values of the full observation
563 record. The QC procedures offered here may be valuable for scientists developing their own QC efforts.

564   We presented examples of time series of air temperature, surface height, atmospheric pressure,
565 snow temperature, surface albedos, and longwave radiation based on the resulting hourly
566 meteorological dataset for 2012–2020 in northwest Greenland. We also extracted information on
567 climatological cloudiness based on LW_net data derived from these in situ ground observations. Our
568 primary findings are summarized in the following four points: (1) in the 2015 summer, high air
569 temperature, in addition, 2016, 2019, 2020 summers low surface albedos were recorded at both
570 SIGMA-A and SIGMA-B sites. (2) Dramatic decreases in surface height occurred in 2015 at both
571 AWS sites and in 2016, 2019, and 2020 at the SIGMA-B site. (3) Weather conditions in JJA were
572 relatively variable in northwest Greenland compared to the other seasons. (4) Clear-sky conditions
573 typified the summers of 2015, 2019, and 2020.

574   The datasets described here are archived in the open access Arctic Data archive System for all
575 scientific communities. We anticipate that they will not only aid in understanding and monitoring the
576 current climate in northwest Greenland but also contribute more broadly to the advancement of polar
577 climate studies.

578

579 **Author contribution**

580   All authors, excluding M. Nishimura, established the AWS systems and supported their
581 maintenance. In addition, M. Nishimura developed and carried out the QC procedures and analyzed
582 the observation data, TA designed and led the study project and provided technical support for the QC
583 procedures, M. Niwano conducted pre-treatments for the meteorological data record and constructed
584 a fundamental algorithm of the QC procedures, TY supported the field observations, especially
585 logistical support, and KF provided advice on interpreting the observational data. All authors
586 participated in the interpretation of results and gave final approval for publication.

587 **Competing interests**

588   The authors declare that they have no conflict of interest.

589 **Acknowledgments**

590   We recognize all members of the SIGMA project, the GRENE-Arctic Project in Greenland, and
591 the Arctic Challenge for Sustainability II (ArCS II) project. We also thank all of those who supported
592 the field observations. In particular, we thank Y. Iizuka (Hokkaido University), Y. Kurosaki (Hokkaido
593 University), and A. Tsushima (Chiba University) for taking part in the field activities at the SIGMA-

594 A site and establishing the AWS and Y. Komuro (National Institute of Polar Research) for technical
595 advice. This study was conducted as a part of the "Snow Impurity and Glacial Microbe effects on
596 abrupt warming in the Arctic (SIGMA)" Project supported by the Japan Society for the Promotion of
597 Science Grant-in-Aid for Scientific Research numbers JP23221004 and JP16H01772, the Global
598 Change Observation Mission-Climate (GCOM-C) research project of the Japan Aerospace
599 Exploration Agency, and ArCS II Program Grant Number JPMXD1420318865. For the use of
600 NunaGIS (http://en.nunagis.gl/) operated by Asiaq, Greenland Survey, in preparing Fig. 1, we
601 acknowledge the National Snow and Ice Data Center's QGreenland package (Moon et al., 2021). The
602 DEM data from Arctic DEMs were provided by the Polar Geospatial Center under NSF-OPP awards
603 1043681, 1559691, and 1542736.

References

605 Aoki, T., Aoki, T., Fukabori, M., and Uchiyama, A.: Numerical simulation of the atmospheric effects
606 on snow albedo with a multiple scattering radiative transfer model for the atmosphere-snow system,
607 J. Meteorol. Soc. Japan, 77, 595-614, https://doi.org/10.2151/jmsj1965.77.2_595, 1999.

608 Aoki, T., Kuchiki, K., Niwano, M., Kodama, Y., Hosaka, M., and Tanaka, T.: Physically based snow
609 albedo model for calculating broadband albedos and the solar heating profile in snowpack for
610 general circulation models. J. Geophys. Res.: Atmos., 116 (D11114), 1–22.
611 https://doi.org/10.1029/2010JD015507, 2011.

612 Aoki, T., Hachikubo, A., and Hori, M.: Effect of snow physical parameters on shortwave broadband
613 albedos, J. Geophys. Res., 108, D19, 1–12. https://doi.org/10.1029/2003jd003506, 2003.

614 Aoki, T., Matoba, S., Uetake, J., Takeuchi, N., and Motoyama, H.: Field activities of the "Snow
615 Impurity and Glacial Microbe effects on abrupt warming in the Arctic" (SIGMA) Project in
616 Greenland in 2011-2013. Bull. Glaciol. Res., 32, 3–20. https://doi.org/10.5331/bgr.32.3, 2014.

617 Armstrong, R. L. and Brun, E. (Eds.).: Physical processes within the snow cover and their
618 parameterization, in Snow and Climate: Physical Processes, Surface Energy Exchange and
619 Modeling, Cambridge University Press, Cambridge N.Y., p. 58, 2008.

620 Behrens, K.: Radiation sensors, in: Springer handbook of atmospheric measurements, edited by: Foken,
621 T., Springer International Publishing, pp. 297–357, https://doi.org/10.1007/978-3-030-52171-
622 4_11, 2021.

623 Braithwaite, R. J. and Olesen, O. B.: A simple energy-balance model to calculate ice ablation at the
624 margin of the Greenland ice sheet. J. Glaciol., 36, 222–228.
625 https://doi.org/10.1017/S0022143000009473, 1990.

626 Brock, B. W. and Arnold, N. S.: A spreadsheet-based (Microsoft Excel) point surface energy balance
627 model for glacier and snow melt studies. Earth Surf. Proc. Land., 25, 649–658.
628 https://doi.org/10.1002/1096-9837(200006)25:6<649::AID-ESP97>3.0.CO;2-U, 2000.

629 Estévez, J., Gavilán, P., and Giráldez, J. V.: Guidelines on validation procedures for meteorological
630   data from automatic weather stations, J. Hydrol., 402, 144–154.
631   https://doi.org/10.1016/j.jhydrol.2011.02.031, 2011.

632 Fausto, R. S., van As, D., Mankoff, K. D., Vandecrux, B., Citterio, M., Ahlstrøm, A. P., Andersen, S.
633   B., Colgan, W., Karlsson, N. B., Kjeldsen, K. K., Korsgaard, N. J., Larsen, S. H., Nielsen, S.,
634   Pedersen, A., Shields, C. L., Solgaard, A. M., and Box, J. E.: Programme for Monitoring of the
635   Greenland Ice Sheet (PROMICE) automatic weather station data. Earth Syst. Sci. Data, 13, 3819–
636   3845. https://doi.org/10.5194/essd-13-3819-2021, 2021.

637 Fiebrich, C. A., Morgan, Y. R., McCombs, A. G., Hall, P. K., and McPherson, R. A.: Quality assurance
638   procedures for mesoscale meteorological data. J. Atmos. Ocean. Tech., 27, 1565–1582.
639   https://doi.org/10.1175/2010JTECHA1433.1, 2010.

640 Fröhlich, C.: Total solar irradiance observations. Surv. Geophys, 33, 453–473.
641   https://doi.org/10.1007/s10712-011-9168-5, 2012.

642 Fujita, K., Matoba, S., Iizuka, Y., Takeuchi, N., Tsushima, A., Kurosaki, Y., and Aoki, T.: Physically
643   based summer temperature reconstruction from melt layers in ice cores. Earth Space Sci.,
644   8(e2020EA001590), 1–17. https://doi.org/10.1029/2020EA001590, 2021.

645 Hirose, S., Aoki, T., Niwano, M., Matoba, S., Tanikawa T., Yamaguchi, S., , and Yamasaki, T.:
646   Surface energy balance observed at the SIGMA-A site on the northwest Greenland ice sheet (in
647   Japanese with English abstract). Seppyo, 83, 143–154, https://doi.org/10.5331/seppyo.83.2_143,
648   2021.

649 Hock, R. and Holmgren, B.: A distributed surface energy-balance model for complex topography and
650   its application to Storglaciären, Sweden, J. Glaciol., 51, 25–36.
651   https://doi.org/10.3189/172756505781829566, 2005.

652 Jonsell, U., Hock, R., and Holmgren, B.: Spatial and temporal variations in albedo on Storglaciären,
653   Sweden, J. Glaciol., 49, 59–68. https://doi.org/10.3189/172756503781830980, 2003.

654 Kim, H. M. and Kim, B. M.: Relative contributions of atmospheric energy transport and sea ice loss
655   to the recent warm arctic winter. J. Clim., 30, 7441–7450. https://doi.org/10.1175/JCLI-D-17-
656   0157.1, 2017.

657 Kurosaki, Y., Matoba, S., Iizuka, Y., Niwano, M., Tanikawa, T., Ando, T., Hori, A., Miyamoto, A.,
658   Fujita, S., and Aoki, T.: Reconstruction of sea ice concentration in northern Baffin Bay using
659   deuterium excess in a coastal ice core from the north-western Greenland Ice Sheet. J. Geophys.
660   Res. Atmos., 125. https://doi.org/10.1029/2019JD031668, 2020.

661 Liang, Y., Bi, H., Huang, H., Lei, R., Liang, X., Cheng, B., and Wang, Y.: Contribution of warm and
662   moist atmospheric flow to a record minimum July sea ice extent of the Arctic in 2020. The
663   Cryosphere, 16, 1107–1123. https://doi.org/10.5194/tc-16-1107-2022, 2022.

664   Makkonen, L. and Laakso, T.: Humidity measurements in cold and humid environments. Boundary-
665   Layer Meteorol., 116, 131–147. https://doi.org/10.1007/s10546-004-7955-y, 2005.

666   Matoba, S., Niwano, M., Tanikawa, T., Iizuka, Y., Yamasaki, T., Kurosaki, Y., Aoki, T., Hashimoto,
667   A., Hosaka, M., and Sugiyama, S.: Field activities at the SIGMA-A site, north-western Greenland
668   Ice Sheet, 2017. Bull. Glaciol. Res., 36, 15–22. https://doi.org/10.5331/BGR.18R01, 2018.

669   Matoba, S., Yamaguchi, S., Tsushima, A., Aoki, T., and Sugiyama, S.: Surface mass balance variations
670   in a maritime area of the north-western Greenland Ice Sheet (in Japanese with English abstract).
671   Low Temperature Science, 75, 37–44, doi: 10.14943/lowtemsci.75.37, 2017.

672   Moon, T., Fisher, M., Harden, L., and Stafford, T.: QGreenland (v1.0.1) [software]. Available from
673   https://qgreenland.org. https://doi.org/10.5281/zenodo.4558266, 2021.

674   Moradi, I.: Quality control of global solar radiation using sunshine duration hours, Energy, 34, 1–6.
675   https://doi.org/10.1016/j.energy.2008.09.006, 2009.

676   Morino, S., Kurita, N., Hirasawa, N., Motoyama, H., Sugiura, K., Lazzara, M., Mikolajczyk, D.,
677   Welhouse, L., Keller, L., and Weidner, G.: Comparison of Ventilated and Unventilated Air
678   Temperature Measurements in Inland Dronning Maud Land on the East Antarctic Plateau. J.
679   Atmos. and Ocean. Technol., 38, 2061–2070. https://doi.org/10.1175/JTECH-D-21-0107.1, 2021.

680   Morrison, H., De Boer, G., Feingold, G., Harrington, J., Shupe, M. D., and Sulia, K.: Resilience of
681   persistent Arctic mixed-phase clouds. Nat. Geosci., 5, 11–17. https://doi.org/10.1038/ngeo1332,
682   2012.

683   Mouginot, J., Rignot, E., Bjørk, A. A., van den Broeke, M., Millan, R., Morlighem, M., Noël, B.,
684   Scheuchl, B., and Wood, M.: Forty-six years of Greenland Ice Sheet mass balance from 1972 to
685   2018, P. Natl. Acad. Sci. USA, 116, 9239–9244. https://doi.org/10.1073/pnas.1904242116, 2019.

686   Nishimura, M., T. Aoki, M. Niwano, S. Matoba, T. Tanikawa, S. Yamaguchi, T. Yamasaki, A.
687   Tsushima, K. Fujita, Y. Iizuka, Y. Kurosaki: Quality-controlled datasets of Automatic Weather
688   Station (AWS) at SIGMA-A site from 2012 to 2020: Level 1.1, 1.00, Arctic Data archive System
689   (ADS), Japan [dataset], http://doi.org/10.17592/001.2022041301, 2023a.

690   Nishimura, M., T. Aoki, M. Niwano, S. Matoba, T. Tanikawa, S. Yamaguchi, T. Yamasaki, A.
691   Tsushima, K. Fujita, Y. Iizuka, Y. Kurosaki: Quality-controlled datasets of Automatic Weather
692   Station (AWS) at SIGMA-A site from 2012 to 2020: Level 1.2, 1.20, Arctic Data archive System
693   (ADS), Japan [dataset], http://doi.org/10.17592/001.2022041302, 2023b.

694   Nishimura, M., T. Aoki, M. Niwano, S. Matoba, T. Tanikawa, S. Yamaguchi, T. Yamasaki, A.
695   Tsushima, K. Fujita, Y. Iizuka, Y. Kurosaki: Quality-controlled datasets of Automatic Weather
696   Station (AWS) at SIGMA-A site from 2012 to 2020: Level 1.3, 1.20, Arctic Data archive System
697   (ADS), Japan [dataset], http://doi.org/10.17592/001.2022041303, 2023c

698   Nishimura, M., T. Aoki, M. Niwano, S. Matoba, T. Tanikawa, S. Yamaguchi, T. Yamasaki, K. Fujita:
699   Quality-controlled datasets of Automatic Weather Station (AWS) at SIGMA-B site from 2012 to

700   2020: Level 1.1, 1.00, Arctic Data archive System (ADS), Japan [dataset],
701   http://doi.org/10.17592/001.2022041304, 2023d.

702 Nishimura, M., T. Aoki, M. Niwano, S. Matoba, T. Tanikawa, S. Yamaguchi, T. Yamasaki, K. Fujita:
703   Quality-controlled datasets of Automatic Weather Station (AWS) at SIGMA-B site from 2012 to
704   2020: Level 1.2, 1.10, Arctic Data archive System (ADS), Japan [dataset],
705   http://doi.org/10.17592/001.2022041305, 2023e.

706 Nishimura, M., T. Aoki, M. Niwano, S. Matoba, T. Tanikawa, S. Yamaguchi, T. Yamasaki, K. Fujita:
707   Quality-controlled datasets of Automatic Weather Station (AWS) at SIGMA-B site from 2012 to
708   2020: Level 1.3, 1.20, Arctic Data archive System (ADS), Japan [dataset],
709   http://doi.org/10.17592/001.2022041306, 2023f.

710 Niwano, M., Aoki, T., Matoba, S., Yamaguchi, S., Tanikawa, T., Kuchiki, K., and Motoyama, H.:
711   Numerical simulation of extreme snowmelt observed at the SIGMA-A site, northwest Greenland,
712   during summer 2012. The Cryosphere, 9, 971–988. https://doi.org/10.5194/tc-9-971-2015, 2015.

713 Niwano, M., Aoki, T., Hashimoto, A., Matoba, S., Yamaguchi, S., Tanikawa, T., Fujita, K., Tsushima,
714   A., Iizuka, Y., Shimada, R., and Hori, M.: NHM-SMAP: Spatially and temporally high-resolution
715   nonhydrostatic atmospheric model coupled with detailed snow process model for Greenland Ice
716   Sheet. The Cryosphere, 12, 635–655. https://doi.org/10.5194/tc-12-635-2018, 2018.

717 Niwano, M., Box, J. E., Wehrlé, A., Vandecrux, B., Colgan, W. T., and Cappelen, J.: Rainfall on the
718   Greenland Ice Sheet: Present-day climatology from a high-resolution non-hydrostatic polar
719   regional climate model. Geophys. Res. Lett., 48(e2021GL092942), 1–11.
720   https://doi.org/10.1029/2021GL092942, 2021.

721 Noël, B., van de Berg, W. J., Lhermitte, S., and van den Broeke, M. R.: Rapid ablation zone expansion
722   amplifies north Greenland mass loss, Sci. Adv., 5, 2–11. https://doi.org/10.1126/sciadv.aaw0123,
723   2019.

724 Onuma, Y., Takeuchi, N., Tanaka, S., Nagatsuka, N., Niwano, M., and Aoki, T.: Observations and
725   modelling of algal growth on a snowpack in north-western Greenland. The Cryosphere, 12, 2147–
726   2158. https://doi.org/10.5194/tc-12-2147-2018, 2018.

727 Porter, C., Morin, P., Howat, I., Noh, M. J., Bates, B., Peterman, K., Keesey, S., Schlenk, M., Gardiner,
728   J., Tomko, K., Willis, M., Kelleher, C., Cloutier, M., Husby, E., Foga, S., Nakamura, H., Platson,
729   M., Wethington, M. Jr., Williamson, C., Bauer, G., Enos, J., Arnold, G., Kramer, W., Becker, P.,
730   Doshi, A., D'Souza, C., Cummens, P., Laurier, F., Bojesen, M.: "ArcticDEM",
731   https://doi.org/10.7910/DVN/OHHUKH, Harvard Dataverse, V1, [Accessed in January 18, 2022],
732   2018.

733 Rottman, G.: Measurement of total and spectral solar irradiance. Space Sci. Rev., 125, 39–51.
734   https://doi.org/10.1007/s11214-006-9045-6, 2006.

735 Ryan, J. C., Smith, L. C., Cooley, S. W., Pearson, B., Wever, N., Keenan, E., and Lenaerts, J. T. M.:
736   Decreasing surface albedo signifies a growing importance of clouds for Greenland Ice Sheet
737   meltwater production. Nat. Comm., 13(4205), 1–8. https://doi.org/10.1038/s41467-022-31434-w,
738   2022.

739 Steffen, C. and Box, J. E.: Surface climatology of the Greenland ice sheet: Greenland Climate Network
740   1995-1999, J. Geophys. Res., 106, D24, 33951–33964, 2001.

741 Stramler, K., Del Genio, A. D., and Rossow, W. B.: Synoptically driven Arctic winter states. J. Clim.,
742   24, 1747–1762. https://doi.org/10.1175/2010JCLI3817.1, 2011.

743 Sugiyama, S., Sakakibara, D., Matsuno, S., Yamaguchi, S., Matoba, S., and Aoki, T.: Initial field
744   observations on Qaanaaq ice cap, north-western Greenland, Ann. Glaciol., 55, 25–33.
745   https://doi.org/10.3189/2014AoG66A102, 2014.

746 Takeuchi, N., Sakaki, R., Uetake, J., Nagatsuka, N., Shimada, R., Niwano, M., and Aoki, T.: Temporal
747   variations of cryoconite holes and cryoconite coverage on the ablation ice surface of Qaanaaq
748   Glacier in northwest Greenland. Ann. Glaciol., 59, 21–30. https://doi.org/10.1017/aog.2018.19,
749   2018.

750 Tanikawa, T., Hori, M., Aoki, T., Hachikubo, A., Kuchiki, K., Niwano, M., Matoba, S., Yamaguchi, S.,
751   and Stamnes, K.: In situ measurements of polarization properties of snow surface under the
752   Brewster geometry in Hokkaido, Japan, and northwest Greenland ice sheet. J. Geophys. Res., 119,
753   13,946-13,964. https://doi.org/10.1002/2014JD022325, 2014.

754 Tsutaki, S., Sugiyama, S., Sakakibara, D., Aoki, T., and Niwano, M.: Surface mass balance, ice
755   velocity and near-surface ice temperature on Qaanaaq Ice Cap, north-western Greenland, from
756   2012 to 2016, Ann. Glaciol., 58, 181–192. https://doi.org/10.1017/aog.2017.7, 2017.

757 van As, D., Fausto, R. S., Ahlstrøm, A. P., Andersen, S. B., Andersen, M. L., Citterio, M., Edelvang,
758   K., Gravesen, P., Machguth, H., Nick, F. M., Nielsen, S., and Anker, W.: Programme for
759   Monitoring of the Greenland Ice Sheet (PROMICE): First temperature and ablation records, Geol.
760   Surv. Den. Greenl., 23, 73–76. https://doi.org/10.34194/geusb.v23.4876, 2011.

761 van den Broeke, M., van As, D., Reijmer, C., and van de Wal, R.: Assessing and improving the quality
762   of unattended radiation observations in Antarctica, J. Atmos. Ocean. Tech., 21, 1417–1431.
763   https://doi.org/10.1175/1520-0426(2004)021<1417:AAITQO>2.0.CO;2, 2004a.

764 van den Broeke, M., Reijmer, C., and van de Wal, R.: Surface radiation balance in Antarctica as
765   measured with automatic weather stations, J. Geophys. Res., 109, D09103, 1–17.
766   https://doi.org/10.1029/2003JD004394, 2004b.

767 van de Wal, R. S. W., Greuell, W., Van den Broeke, M. R., Reijmer, C. J., and Oerlemans, J.: Surface
768   mass-balance observations and automatic weather station data along a transect near Kangerlussuaq,
769   West Greenland. Ann. Glaciol., 42, 311–316. https://doi.org/10.3189/172756405781812529, 2005.

770 Wehrli, C.: World Radiation Center (WRC) Publication. Davos-Dorf, Switzerland, 615, pp. 10-17,
771   1985.

772 Wiscombe, W. J., and Warren S. G.: A model for the spectral albedo of snow. I, Pure snow. J. Atmos.
773   Sci., 37, 2712–2733., 1980.

774 Yamaguchi, S., Matoba, S., Yamazaki, T., Tsushima, A., Niwano, M., Tanikawa, T., and Aoki, T.:
775   Glaciological observations in 2012 and 2013 at SIGMA-A site, Northwest Greenland. Bull.
776   Glaciol. Res., 32, 95–105. https://doi.org/10.5331/bgr.32.95, 2014.